Mars' ionospheric interaction with comet C/2013 A1 Siding-Spring's coma at their closest approach as seen by Mars Express

Beatriz Sánchez–Cano[1], Mark Lester[1], Olivier Witasse[2], David D. Morgan[3], Hermann Opgenoorth[4,1], David J. Andrews[5], Pierre-Louis Blelly[6], Stanley W.H. Cowley[1], Andy Kopf[3], Francois Leblanc[7], Jared R. Espley[8]

[1] Radio and Space Plasma Physics Group, Department of Physics and Astronomy, University of Leicester, University Road, Leicester, LE1 7RH, UK.

[2] European Space Agency, ESTEC – Scientific Support Office, Keplerlaan 1, Noordwijk 2200 AG, The Netherlands.

[3] Department of Physics and Astronomy, University of Iowa, Iowa City, IA, USA

[4] Department of Physics, Umeå University, Linnaeus väg 24, 901 87 Umea, Sweden

[5] Swedish Institute of Space Physics, Uppsala, Sweden

[6] Institut de Recherche en Astrophysique et Planétologie (IRAP), Toulouse, France.

[7] LATMOS/CNRS, Sorbonne Université, UVSQ, Paris, France

[8] NASA Goddard Space Flight Center, Greenbelt, Maryland, USA

Corresponding author: Beatriz Sánchez-Cano (bscmdr1@leicester.ac.uk)

Key Points:

- We analyze the Mars Express-MARSIS observations of the interaction between Mars' ionosphere and comet Siding Spring at closest approach
- Large Martian ionospheric variability is observed during the closest approach with comet Siding-Spring
- Cometary water, dust and comet induced magnetic field seem to be equally responsible for the large ionospheric density variability

Key Words: ionosphere, Mars, comet Siding-Spring, Mars Express

Abstract

On 19 October 2014, Mars experienced a very close encounter with Comet C/2013 A1 Siding Spring. Using data from the Mars Advanced Radar for Subsurface and Ionosphere Sounding (MARSIS) on board Mars Express (MEX), we assess the interaction of the Martian ionosphere with the comet's atmosphere and possibly magnetic tail during the orbit of their closest approach. The topside ionospheric electron density profile is evaluated from the peak density of the ionosphere to the local plasma around Mars Express. We find unusual, complex and rapid variability in the ionospheric profile along the MEX orbit, not seen even after the impact of large coronal mass ejections. Before closest approach, large electron density reductions predominate, which could be caused either by comet water-damping, or comet magnetic field interactions. After closest approach, a substantial electron density rise predominates. Moreover, several extra topside layers are visible along the whole orbit at different altitudes, which could be related to different processes as we discuss.

Plain Language Summary

The comet Siding-Spring made a single flyby through the Solar System in October 2014, passing very close to Mars on 19 October 2014. For about 10h, the Martian ionosphere (upper atmosphere) was in touch with the cometary atmosphere, also called the coma. In this work, we use data from the Mars Express mission to evaluate the behavior of the ionosphere of Mars at the comet closest approach. We find that the Martian ionosphere suffered a very quick and complex variability with very large density increases and decreases every few kilometers. This variability was caused by the presence of the comet, and we discuss different processes that could have occurred.

1. Context and Motivation

In October 2014, we were witness to an exceptional planetary event in which the atmosphere of a planet was in direct contact with the atmosphere of a comet. This unique event during the space age took place when the Oort-cloud comet named Comet C/2013 A1 (hereinafter Siding Spring) flew by Mars at a distance of only 138,000 kilometers (41.4 Mars radii) during a single flyby through the inner Solar System. Its water production rate at Mars was estimated with in-situ and remote sensing instruments at $1.1\text{-}1.5\pm0.5\times10^{28}$ molecules s^{-1} (Crismani et al., 2015; Schleicher et al., 2014; Bodewits et al., 2015).

Several teams have published different aspects of the Martian atmospheric and ionospheric behavior well after Siding Spring's flyby (few hours after), when the cometary dust had been deposited into the Martian atmosphere. In particular, a total dust mass of 82±25 t was deposited in Mars' atmosphere, creating an ionospheric layer of Mg^+ and Fe^+ between 105 and 120 km altitude (Crismani et al., 2018; Benna et al., 2015; Schneider et al., 2015) as measured by the Mars Atmosphere and Volatile Evolution (MAVEN) mission. This layer was also observed by the Mars Advanced Radar for Subsurface and Ionosphere Sounding (MARSIS) on board Mars Express (MEX) (Gurnett et al., 2015; Venkateswara et al., 2016) for two days after the comet encounter. Indeed, this is the largest meteor layer ever observed at a planet other than Earth (Gurnett et al., 2015). In addition, a large total electron content (TEC) increase was recorded by the Mars Reconnaissance Orbiter (MRO) (Restano et al., 2015). The comet also produced large magnetic turbulence in the Martian ionosphere and magnetosheath that lasted several hours after the comet departed (Espley et al., 2015).

However, the interaction of the planetary and cometary atmospheres at the time of the closest approach (CA) is largely unknown. One of the main reasons is that all the spacecraft were placed into a protective mode to avoid as much as possible dust impacts from comet sputtering, as dust travelled at the same highly super-sonic speed of the comet, 56 km s^{-1}. For example, the trajectory of MEX was placed such that the spacecraft was mostly protected from the dust by being behind the planet during the comet encounter (from the debris perspective), while MAVEN had most of its payload switched-off having only recently arrived at Mars (the geometry of the encounter is described in the next two sections). In addition, most of the plasma observations during the encounter were very challenging to analyze because 44 h before, a large interplanetary coronal mass ejection (ICME) hit Mars (Witasse et al., 2017), and a large shower of energetic particles into the ionosphere from both the comet and the solar wind was observed at Mars for several days (Sánchez-Cano et al., 2018).

Despite these difficulties, there are many data sets still to exploit. The objective of this paper is to examine the MARSIS-MEX dataset at the time of CA before dust had settled in the atmosphere (MEX orbit 13709), and assess the behavior of the Martian ionosphere during its interaction with Siding Spring's coma.

2. Geometry of the Encounter

Figure 1 shows three different views of the geometry of the encounter at CA, where Siding Spring has been represented as a sphere of radius 15000 km for better visualization (the comet size is only few kilometers). At the time of the encounter with Mars, Siding Spring was moving from the south to the north of the ecliptic plane in a hyperbolic orbit (129° inclination angle) and with a relative speed of ~56 km s^{-1} (JPL Small-Body Database, https://ssd.jpl.nasa.gov/sbdb.cgi?). The CA with Mars occurred at 18:28 UT on 19 October 2014, when the Siding Spring nucleus located relative to the North-Dawn sector of Mars.

The comet had a near circular atmosphere (or coma) surrounding the nucleus that can be considered the size of a million kilometers from the comet's nucleus which entirely engulfed Mars for ~10 h (Espley et al., 2015; Sánchez-Cano et al., 2018). The entire MEX orbit 13709 occurred when Mars was inside the coma. In addition, as a typical comet, Siding Spring had two different tails that extend millions of kilometers. The dust tail, which is formed by material from the surface and coma that is blown away due to solar radiation pressure, hit the Martian Southern hemisphere. Figure 2 shows the relative positions of Mars, MEX and Siding Spring at CA. During CA, Mars was partly blocking the dust stream and forming a shadow area for dust impacts in the Northern hemisphere (reddish cylinder in Figure 2b, positions p1 and p2 in Figure 2a), where MEX was placed for security. Therefore, due to their relative position, the Martian southern hemisphere near the morning terminator was the most affected by cometary dust, as this hemisphere was facing toward the cometary particle motion at CA. The peak dust flux was predicted to occur at ~20:06 UT on 19 October (Tricarico et al., 2014) when Mars crossed the comet's orbital plane. In addition to the dust tail, the ion tail also hit Mars for a short period of time. This tail is formed of pickup ions that have joined the flow of the solar wind, adding mass to it and decelerating it, and is surrounded by draped solar wind magnetic field (cometary magnetosphere). Therefore, it is found in opposite direction to the Sun-comet interaction. In principle, Mars was affected by the head of the cometary magnetosphere at CA as we discuss in section 5.

3. MARSIS Dataset and MEX attitude

In this work, we use data from the MARSIS instrument (Picardi et al., 2004; Orosei et al., 2015) on board MEX (Chicarro et al., 2004). MARSIS is a radar that can work in two different operational modes. The first mode is designed to sound the surface and sub-surface of the planet, while the second mode, called Active Ionospheric Sounding (AIS), is designed to sound the topside of the ionosphere of Mars. In this study, we use the MARSIS-AIS dataset that provides electron density profiles of the topside ionosphere (~130-350 km) (e.g. Sánchez-Cano et al., 2012; Morgan et al., 2013). In addition, the AIS dataset also provides information on the spacecraft surroundings (hereinafter referred to as the local plasma) depending on MEX altitude (between ~350 and ~1000 km). Specifically it provides the electron density from the excitation of local electron plasma oscillations, and the magnetic field magnitude from the local cyclotron frequency (e.g. Gurnett et al., 2005; 2008; Akalin et al., 2010; Andrews et al., 2013). The magnetic field measured by MARSIS could originate either from crustal magnetic fields on the Martian surface, or be induced from the solar wind (draped solar wind magnetic field), or both. In this study, we assume that only an induced magnetic field is present in the MARSIS records as MEX was flying above the Northern hemisphere at the time of the MARSIS observations, far from the most intense crustal fields.

During an orbit periapsis, MEX typically points toward the planet. However, during the comet encounter, the MEX attitude was different due to operational reasons (the spacecraft was upside down). Fortunately, this issue does not affect MARSIS in AIS mode measurements because the pulses sent out by the instrument propagate roughly spherically in all directions. As a result, the initial reflections always come from the ionosphere via the shortest propagation path which is typically from vertical echoes. Any slant path transmissions will generally not return to the spacecraft, unless the ionosphere is not smooth and there are oblique echoes (e.g., Gurnett et al., 2005; Duru et al., 2006; Andrews et al., 2014).

4. Observations

4.1. Ionosphere between 350 and 1000 km

Figure 3 presents the local ionospheric plasma observations at MEX altitude for the orbit of the comet encounter, 13709, as well as for the four previous and three following orbits. For orientation, Figure 3a shows the MEX trajectory during this period. The MEX path through the ionosphere's cavity (below the magnetic pileup boundary) is represented in green, with MEX moving from the North Pole towards the equator, and crossing the day-night terminator from the

night to the dayside. Figures 3d-3k show the local electron density and the magnitude of the local magnetic field for consecutive orbits. Since these are observations taken locally at the spacecraft position, they are altitude and solar zenith angle (SZA) dependent. This means that the local electron density should be larger at MEX's pericenter (marked with a P) than at higher altitudes, and also larger for lower SZA (dayside). As mentioned before, the Martian plasma system was affected by an ICME that impacted the planet 44h before the comet encounter. Therefore, in order to help with the analysis, two additional panels have been added showing the local plasma observations for solar wind steady conditions before the ICME hit Mars (Figure 3b), and for the orbit right after the impact of the ICME (Figure 3c). The letters A and B at the top of each panel indicate the start/end of MARSIS detections of electron density above zero, as a proxy for the length of the passage through the ionosphere.

For steady solar wind conditions, one expects similar observations to those in Figure 3b as the MEX trajectory does not change very much over the course of a few days. A gradual density increase occurs until pericenter as MEX moves from the night to the dayside and reduces in altitude. It continues to increase after pericenter as MEX is on the dayside and SZA increases. Then there is a plateau for several minutes while MEX ascends and SZA descends until a rapid decrease to lower values occurs, which is typically identified with the transition across the pileup boundary and into the sheath. The magnetic field remains nearly constant at 20 nT for the whole ionospheric transit. However, the scenario is very different after the impact of an ICME. Figure 3c shows a large rise of magnetic field magnitude that remains at 60-80 nT for most of the orbit. It also shows a significant local electron density reduction, with values near 0.5 cm^{-3} at the pericenter, and a sudden increase after periapsis that lasts a minute, where a density of ~3500 cm^{-3} is reached. This brief density increase can be associated with the only moment in which MEX transited the proper ionosphere (denser part). The size of the ionosphere passage is largely reduced (see A-B positions) when compared to steady conditions, which means that the ionosphere occurred at lower altitudes than normal. This is due to a large compression of the ionosphere as a result of the ICME passage.

Figures 3d-3g show local plasma observations during the recovery of the ICME impact, and just before the Siding Spring flyby (Figure 3h). The magnitude of the magnetic field is reduced from orbit to orbit, while the ionospheric densities gradually become more similar to those in the steady ionosphere (panel b). We note that orbit 13708 (Figure 3g) shows an irregular behavior. The normal transit to the ionosphere occurs between positions A and B, having a sharp density decrease after periapsis that indicates that MEX left the ionosphere (position B). However, there is a moderate increase in density several minutes later when MEX was higher than 700 km, coming back into the ionospheric regime (A*-B*). This is due to a short magnetosheath transit

between the positions B and A* most probably caused by a magnetosheath-boundary motion (see e.g. Sánchez-Cano et al., 2017).

Figure 3h shows Mars' ionosphere observations at the time of Siding-Spring's CA. These observations are very intriguing as the ionosphere is unusually rarified. MEX density observations at the pericenter are as low as after the passage of the ICME (see Figure 3c for comparisons). However, the size of the MEX ionospheric passage (A-B distance) was standard, and the magnitude of the magnetic field was ~30-40 nT which is close to that for steady conditions and similar to previous orbits. MARSIS-AIS observations indicate that the magnetosheath turbulence found by Espley et al. (2015) during this time did not affect the size of the ionospheric cavity. This means that the magnetic and dynamic pressures exerted by the comet were not enough to move the magnetosheath to lower altitudes as always happens with an ICME. So, in summary, MEX was in the ionosphere from A to B/B*, but between A and 18:27 the electron densities were strongly suppressed. From 18:27 till 18:32, a notable density increase is observed up to ~1500 cm^{-3}, which is not typical for altitudes larger than 700 km in steady conditions. The post-flyby orbit (Figure 3i) also shows a similar level of ionization for similar altitudes, but in this case the cause must be related to the dust deposition within the atmosphere, as corroborated by Benna et al. (2015), who also found several species of metal ions in Mars' atmosphere at similar altitudes with MAVEN observations at the same time as Figure 3i. The sharp density decrease at ~18:32 (letter B) in Figure 3h most probably corresponds to MEX crossing into the magnetosheath region, although our analysis is not conclusive since some ionospheric plasma density is still visible until B*.

Figures 3i-3k show the local plasma observations for the orbits after the comet encounter. The post-flyby orbit shows a very robust ionosphere both on the day and nightsides most probably formed by cometary dust deposition. The size of the ionospheric passage is maintained similar to the pre-comet flyby and steady condition orbits, and the level of magnetic field is similar to previous orbits. After that, the ionosphere starts to recover as the density and magnetic field values gradually become normal. The system seems to be recovered by Figure 3k when the longest ionospheric passage of the period is observed.

To summarize, the system seems fully recovered from the ICME impact by orbit 13706 (~21 h before CA) in agreement with MAVEN magnetic observations (Espley et al., 2015). During orbit 13709, when Mars was inside the outer coma of the comet, there is a notable density decrease up to 18:27 UT (just a minute before CA). At 18:27 UT, local plasma density starts to increase and remains high after CA. The orbit after comet-flyby shows very large local density values for the

whole orbit. The system seems to be back to normal conditions by orbit 13712, as seen from MARSIS local plasma parameters.

4.2. Ionosphere between 130 and 350 km

We now focus on the analysis of MARSIS-AIS topside electron density profiles at CA (same orbit as Figure 3h). Similar to the local plasma density, the topside ionosphere also had a very variable behavior. In order to evaluate this electron density variability along the orbit, we use the NeMars model (Sánchez-Cano et al., 2013; 2016a) to compare with the observations. NeMars is an empirical model that describes the electron density distribution with altitude in Mars' ionosphere with respect to SZA, solar activity and heliocentric distance. It is based on Chapman theory adapted to Martian conditions using MARSIS-AIS data. NeMars is ideal for comparisons with these electron density profile observations, as previously demonstrated by other studies such as in support of in-situ Mars crosslink radio-occultations (Ao et al., 2015), solar cycle variations in the Martian ionosphere (Sánchez-Cano et al., 2015b; 2016a; 2016b), annual and solar cycle TEC behavior (Sánchez-Cano et al., 2015a; Cartacci et al., 2018), and ionospheric removal for radar surface studies (Ilyushin et al., 2017).

The electron density profile inversions from the ionograms are implemented according to Morgan et al. (2013) and Sanchez-Cano et al., (2012). We note that there is an alternative inversion made by Němec et al. (2017), which is perhaps better for high altitudes (above ~325 km) because they used MAVEN observations to fill the gap that MARSIS is not able to sample due to the low power emissions at low frequencies. Instead, Morgan et al. (2013) and Sanchez-Cano et al. (2012) use an empirical shape composed of an exponential dependence. However, NeMars was built based on the Morgan et al. (2013) inversion, and therefore, in order to have consistent comparisons, we prefer to keep the original inversions. Nevertheless, in this study, we do not show data above ~325 km in order to minimize the uncertainty. In addition, we only use data with SZA<85° because the model only works for dayside conditions.

Figure 4 shows four MARSIS-AIS topside electron density profiles (blue lines, panels a-d) within less than 8 minutes, and their corresponding NeMars profiles (black dashed lines). These four examples are representative of the overall ionospheric variability observed during orbit 13709. In addition, the corresponding ionograms from which the profiles are retrieved are shown in panels e-h. The first and second profiles (a and b) have a normal behavior from the peak up to 200 km (photochemical region). However, they display a significant density decrease above 200 km (diffusion region) as compared to the model density profile. On the contrary, the third and

fourth profiles (c and d) display a very different ionospheric behavior only a few minutes later. In both cases, the peak altitude is higher than expected, but the density has the same slope as the model up to 200 km (same scale height). However, a significant electron density increase is observed above 200 km, in which several transient ionospheric layers are observed (e.g., at 230 and 260 km in panel c and at 250 km in panel d). This is also observed on their respective ionograms (panels g and h), where a cusp structure is clearly seen at ~1.8 MHz. These extra topside layers are a known phenomenon in Mars' upper ionosphere, first reported by Gurnett el al. (2008) and Kopf et al. (2008), but whose explanation is not straightforward. Peter et al. (2014) indicated that changes in the recombination rate (and thus in the electron density) associated with vertical transport and increase in the electron temperature could be the cause. Kopf et al. (2017) recently suggested that these extra layers are related to local current sheets in the upper Martian ionosphere, which could be related to Kelvin-Helmholtz instabilities, magnetic flux ropes, magnetic reconnection, or solar wind magnetic field rotations.

Figures 5a and 5b present all electron density profiles that could be retrieved from the orbit of the CA (13709), as well as the expected altitude of the main ionospheric peak (gray dashed-line) from the model. To perform a sensible comparison avoiding the normal variability associated with SZA, the relative electron density differences between the AIS observations and the corresponding NeMars value for each data condition are color-coded. Reddish colors indicate an excess of density with respect to the model while blueish colors indicate a reduction. In particular, NeMars was run as normal in Figure 5a, while in Figure 5b the model was fixed by the observed peak electron density. Both panels show the variability of this set of profiles but focusing on different aspects: Figure 5a emphasizes density changes at all altitudes, and Figure 5b highlights scale height changes. To support the observations, the peak electron density, topside TEC, local plasma density from Figure 3h, as well as the MEX altitude, latitude and SZA are shown in Figures 5c-5f, respectively.

In general, the topside ionosphere is found to be much less dense than expected. In the photochemical region (below ~200 km), most of the profiles do not show a large variation with respect to the expected densities (shades of white in Figure 5a), with few exceptions at ~18:21, ~18:23, ~18:26 and ~18:30 UT. Also, they do not show a large variation in scale height (shades of white in Figure 5b) with the exception of a large reduction between ~18:21 and ~18:22 UT and ~18:23 and ~18:26 UT. The largest variations occur within the diffusion region above ~200 km. Large density reductions (up to 40% in some cases) are observed from ~18:19 till 18:24 UT and from 18:25 till 18:27 UT in Figure 5a. They occur at low northern latitudes, on the dayside, and at the same time as the local plasma density (Figure 5e) and TEC reductions (Figure 5d). This

suggests that the complete dayside ionospheric structure above the photochemical region sampled by MEX was affected by the comet.

However, in the course of a few minutes, the ionosphere also showed notable density increases. The most moderate increase occurred between ~18:18 and 18:19 UT coinciding with a significant local density rise (Figure 5a). During this time, the largest density variations occurred at ~210-250 km, which indicates that transient layers similar to Figure 4c were present. There was another moderate increase above ~210 km between ~18:24 and 18:25 UT although the local plasma density remained very low and the scale height (Figure 5b) was smaller than the model. This means that these profiles had a shape similar to that of the first and second profile in Figure 4 but lifted to higher altitudes. The largest density variations occurred from ~18:27 UT onwards when MEX was above 500 km flying at low northern latitudes and lower SZA, coinciding with an increase in local plasma density (Figure 5e). During this period (~18:27 UT onwards), the ionospheric density was raised by at least 40% in most of the profiles. These increases were mostly observed at ~230-260 km altitude, indicating the presence of several transient layers as in Figure 4.

Another important aspect to consider is the ionospheric peak density variability. In general, this parameter is very stable along an orbit having values typically very close to those predicted. Figure 6 compares the peak electron density of the CA orbit (13709, circles in blue) and the orbit before the comet encounter (13708, stars in yellow). During the CA orbit, an unusual large variability is observed along the whole orbit with significant density rises that contrast with the relatively smooth behavior of the pre-comet flyby orbit. This variability is most likely caused by the comet interaction with the Martian atmosphere and solar wind, and not by the transit of the ICME because the system seems totally recovered in previous orbits as shown by several parameters, i.e. normal ionospheric peak behavior (Figure 6 yellow stars), recovered local plasma observations (Figure 3g), and also normal magnetospheric conditions (Espley et al., 2015).

5. Discussion: What Caused the Large and Sudden Martian Ionospheric Variability?

In the course of a few minutes, the ionosphere of Mars showed very unusual and variable behavior with large density increases and reductions that seem not to be related to the typical variability sources, i.e. changes in solar flux or neutral atmospheric conditions. In this section, we discuss possible drivers of this variability.

5.1. Density increase after 18:27 UT

Particles in the coma and dust tail followed the trajectory of the comet at highly super-sonic speeds, moving altogether at the speed of the comet 56 km s^{-1}. Since at CA Mars was completely engulfed by the comet's coma, the whole planet was affected by different cometary particles (e.g. Crismani et al., 2015; 2018; Gurnett et al., 2015; Sánchez-Cano et al., 2018). However, the southern dawn hemisphere was in fact much more affected because it faced towards the cometary dust particle motion. Figure 2a shows four Mars-MEX instants as seen from Siding Spring field-of-view, and Figure 2b shows the relative position of Mars, MEX and Siding Spring from the comet velocity reference frame. In order to protect the spacecraft and their instruments from particle debris impacts, MEX was located above the northern hemisphere and dusk sector during the CA (shadow cylinder area in Figure 2b). This mean that although still affected by the coma, it was in the least risky place with respect to debris impacts because Mars itself acted as a shield for those particles. However, the shielding only lasted for part of the orbit, resulting in MEX encountering the debris stream from 18:25 UT (see MEX position outside the shadow cylinder in Figure 2b, and positions p3-p4 in Figure 2a), and coinciding with the density enhancements in both local plasma and density profiles.

As described before, most of the density enhancements come from extra layers in the topside ionospheric profiles, which could be caused by plasma instabilities, dust ablation, or different energy pick-up ions. We note that these transient layers are identified and retrieved from the ionograms where the ionospheric trace exhibits a cusp structure (see an example in Figure 4g-h). This type of structure corresponds to a nonmonotonic form, for which standard inversion schemes are not set up. Therefore, the electron density profile inversion obtained here is just an indication of a change in those regions and may not be entirely precise. In addition, the uncertainty at high altitudes can propagate to lower altitudes, biasing the peak altitude to too larger values.

Plasma instabilities caused by the relative velocity between the Martian ionosphere and the cometary coma could be the cause for these extra topside layers as in e.g. Kopf et al. (2017). Unfortunately, we do not have enough observations to analyze this scenario. Other potential factors that could have helped in the formation of a denser ionospheric region are MEX travelling within lower SZAs and more equatorial latitudes (i.e. near the area most affected by dust particles), or that Mars was in the densest possible part of the transited coma at this time (i.e., CA). In addition, as said before, we note that the existence of an overhang in the ionospheric trace (e.g. Figure 4g-h) might lead to underestimating the altitude of the ionospheric peak in the electron density profile.

Dust ablation in the atmosphere could be a cause for this density increase. Dust ablation is expected to settle below the main ionospheric peak (~90-100 km), but can also have an effect at higher altitudes when precipitating. However, Crismani et al. (2018) found in a comprehensive analysis that the meteor shower lasted less than 3 h, was limited to one hemisphere, and that horizontal winds globally redistributed this material over the next two days. Benna et al. (2015) also found that ~20h after the flyby, several metallic ions were present at 185 km altitude, which could have been transported by eddy and ambipolar ion diffusion from ~115 km up to 185 km. This phenomenon can explain the large local density values observed during the post-flyby orbit (Figure 3i). However, we do not think the extra topside layers during CA could have been formed almost immediately by this process, since MEX was not in the most affected region (Figure 2b). At CA the atmosphere will have only been in reasonably dense coma for a few tens of minutes, which gives not enough time for redistribution.

Pickup ions from the solar wind could be another feasible scenario. Sánchez-Cano et al. (2018) indicated that for the ~10h period that Mars was at less than a million kilometer distance from the comet, a significant amount of oxygen pickup ions entered Mars' atmosphere, with the pickup ion flux maximizing at CA. The simulation performed by Sánchez-Cano et al. (2018) indicates that O^+ particles with energies of 1 keV were deposited in Mars' atmosphere between 140 and 160 km, having a secondary energy loss peak at ~170 km. However, the energy loss associated with O^+ pickup ions with energies of 1 keV and lower may not be enough to produce a significant electron density increase in Mars' ionosphere (e.g. Wang et al., 2016), as well as one should expect that generally, O^+ pickup ions will be higher energy. In addition, higher energetic O^+ pickup ions were predicted to be deposited lower in the ionosphere. These particles are an important source of atmospheric heating and ionization when they precipitate and lose their energy in Mars' atmosphere. Although difficult to observe with the limited instrumentation that was in operation during CA, the extra density observed at the ionospheric peak (reddish colors) in several profiles of Figure 5a could be related to those energetic pickup ions.

We conclude that MEX encountering the debris stream as well as pick-up ions seem plausible scenarios for explaining these large electron density increases after 18:27 UT, near the time of CA. Unfortunately, the lack of observations at CA does not allow us to get a firm conclusion. More detailed ionospheric modelling of dust and pick-up ion deposition is needed to get more insights on how Mars' ionosphere behaved.

5.2. Density decrease before 18:27 UT

The large density reduction observed at high altitudes during the start of the orbit until 18:27 UT occurred when MEX was shielded by Mars from the cometary debris stream (Figure 2), but still affected by the coma. For those illumination conditions, as well as spacecraft altitude and planetographic conditions, electron density observations should be similar to the NeMars predictions as for the previous orbit. A possible reason is that the coma shielded Mars' atmosphere from some solar extreme-ultraviolet (EUV) wavelengths. Since MARSIS detected the ionospheric peak at a typical density level, only the less energetic EUV fluxes would be affected, and therefore, less ionization would occur at high altitude. However, this hypothesis is unlikely to be the reason because previous studies have found that comets with a similar production rate and closer to the Sun (at 1 AU), do not attenuate the solar EUV flux even at close distances to the nucleus (Bhardwaj, 2003; Vigren and Galand, 2013). This effect is expected to be even smaller for Mars' distance.

Induced magnetic fields from the solar wind can produce density reductions in the topside ionosphere (e.g. Russell and Vaisberg, 1983). During CA, a magnetic field of ~30-40 nT was present at MEX altitude that could be enough to compress the topside profile (e.g. Morel et al., 2004; Sánchez-Cano et al., 2015b; Ramírez-Nicolás et al., 2016). If we assume that the magnetic field is only from the solar wind, this hypothesis seems unlikely because the field is of the same level as previous orbits and only slightly larger than for steady conditions. If this field was responsible, all topside profiles from previous orbits should show a similar behavior, which is not the case. However, we have to consider that the local magnetic observations for orbit 13709 are a mix of solar wind and cometary magnetic fields, which in turn are a distorted version of the draped solar wind magnetic field. Espley et al. (2015) indicate that at CA, a strong rotation of the in-situ magnetic field was observed by MAVEN as the comet approached, draping the cometary magnetic field over Mars. Although we do not have an estimation of the radius of the comet magnetic tail, it can be assumed that the magnetic rotation observed by Espley et al. (2015) is a consequence of the comet magnetic tail interaction with Mars, as Mars was at $\sim 10^5$ km of the nucleus during CA. The ionospheric magnetic field observed by MAVEN experienced several small-scale magnetic field structures with excursions up to 45 nT (Espley et al., 2015), which confirms MARSIS observations of local magnetic field variability (Figure 3h). Consequently, these small-scale magnetic distortions caused most probably by the comet magnetic tail interaction could be a reasonable cause for the somewhat disordered ionospheric reductions observed by MARSIS. Unfortunately, MEX does not have a proper magnetometer for in-situ comparisons.

Other possible reasons are cometary dust and gas interaction with the Martian atmosphere as they are the main component of the coma. Focusing on the dust first, electrons within the ionosphere can be lost due to dust attachment. This is well-known at low and mid altitudes in the Martian atmosphere, especially on the nightside where aerosols tend to negatively charge due to electron attachment when the level of suspended Martian dust is high (Cardnell et al., 2016). Preliminary results from the Planetary Fourier Spectrometer (PFS) (Formisano et al., 2005) on board Mars Express indicate an increase of dust in the Martian atmosphere after the comet's closest approach, especially in the latitude range 40°S-10°N (Giuranna et al., 2017). However, MAVEN observed that ~82 t were deposited in Mars' atmosphere over ~3h and limited to the Martian hemisphere facing the comet (the opposite hemisphere to where MEX was) (Crismani et al., 2018). Although dust within the coma could still have interacted with the ionosphere which was transited by MEX, and have some localized effects, it seems unlikely to be the main cause of the ionospheric reduction.

Water is the other main component of the coma, such that electron dissociative recombination caused by water molecules could be another plausible cause for the observed reduction in electron density. Yelle et al. (2014) predicted that cometary water molecules would penetrate into the Martian atmosphere to an altitude of ~150 km and would most likely be the major source of variability from the coma at high altitude. The influx of cometary water would produce a significant hydrogen increase as a consequence of multiple chemical reactions that eventually reduce the density of ionospheric electrons at those altitudes and above (see reactions R8, R9, R12 and R16 of Yelle et al., 2014). The same phenomenon, but with different chemistry, has been observed at Earth during rocket launches, which introduce a large abundance of H_20, H_2 and CO_2 molecules into the upper ionosphere, resulting in sudden electron density reductions (e.g. Mendillo et al., 1975; 1981). These electron density reductions are very fast, lasting as long as the water source is present. A similar process has also been observed at Saturn, where water-based showers from the rings reduce the electron density of the equatorial Saturnian ionosphere (O'Donoghue et al., 2013; Moore et al., 2015). Moreover, the impact of comet P/Shoemaker–Levy 9 with Jupiter in 1994 also produced a localized significantly reduction of the ionospheric H_3^+ emissions (e.g. Kim et al., 1996), which modelling confirmed to coincide with electron density reductions on the same areas right after the impact. Modeling suggests that cometary water was the cause for both electrons and H_3^+ reductions (Maurellis and Cravens, 2001). Based on MAVEN observations, Crismani et al. (2015) determined that Siding Spring deposited a total mass of 24 t of water gas in Mars' atmosphere, and that cometary hydrogen delivered to the planet from water and its products was $3.4\pm1.7\times10^{12}$ atoms/cm^2, which is comparable with but smaller than the Martian hydrogen abundance above 150 km. Although a global perturbation seems implausible

in terms of the total mass deposited into the whole Mars' atmosphere, the coma is very rich in water species that expands for at least a million kilometers surrounding the comet and could have had a notable damping effect in Mars' atmosphere during the ~5 h that Mars was immersed in the coma. Therefore, in the region not directly affected by comet sputtering (shadow cylinder in Figure 2b), it is reasonable to consider that some localized effects could occur similar to those fast reductions observed at the rocket's launches at Earth which in turn would explain the high variability observed in Mars' ionosphere.

Therefore, we conclude that either cometary magnetic field or water-damping seem plausible scenarios for explaining these large electron density decreases before 18:27 UT, although water seems the more favorable scenario based on previous cometary encounters, such as comet P/Shoemaker–Levy 9. The lack of observations does not allow us to get a firm conclusion, but more detailed ionospheric modelling could be a reasonable next step to understand this behavior.

6. Conclusions

We assess the interaction of the Martian ionosphere with comet Siding Spring's coma and magnetic tail during the orbit of their closest approach, when both atmospheres where in direct interaction. The study employs Mars Express MARSIS observations from orbit 13709 on 19 October 2014 at ~18:30 UT, closest approach compared with surrounding orbits. During this time, the ionosphere of Mars showed very unusual behavior, having an extreme variability not seen even after the impact of large ICMEs.

The ionospheric behavior is evaluated through local plasma observations (electron density and magnetic field intensity local to the spacecraft), as well as though electron density profiles of the ionosphere determined by topside sounding (~130-350 km). We find a very complex and rapid variability along the Mars Express orbit at all altitudes, not typical of this area and solar illumination conditions, which is also not related to space weather activity. Before closest approach, large density reductions predominate above 150 km while after closest approach, a substantial density rise prevails at all altitudes. Moreover, several extra topside layers are visible along the whole orbit at different altitudes. We have discussed different causes for this elevated ionospheric variability, especially the large density reduction, which seems more plausible to be caused by comet water-damping.

The single flyby of comet Siding-Spring to Mars produced massive effects on its ionosphere on a global scale. Therefore, understanding the interaction of the atmosphere/ionosphere of both

483 bodies is very important in order to assess early Mars, as well as the evolution of terrestrial planet
484 atmospheres from times in which comet flybys and impacts occurred more often than now.

485

486 **Acknowledgments**

487 B.S.-C., M.L. and S.W.H.C. acknowledge support through STFC grant ST/S000429/1, and B.S.-C also
488 from the ESA-ESTEC Faculty. Authors are also grateful to the MARSIS-PIs for making the dataset
489 available for the community, and to the ESA-MEX team. All data can be downloaded from the ESA
490 PSA archive.

491

492

493

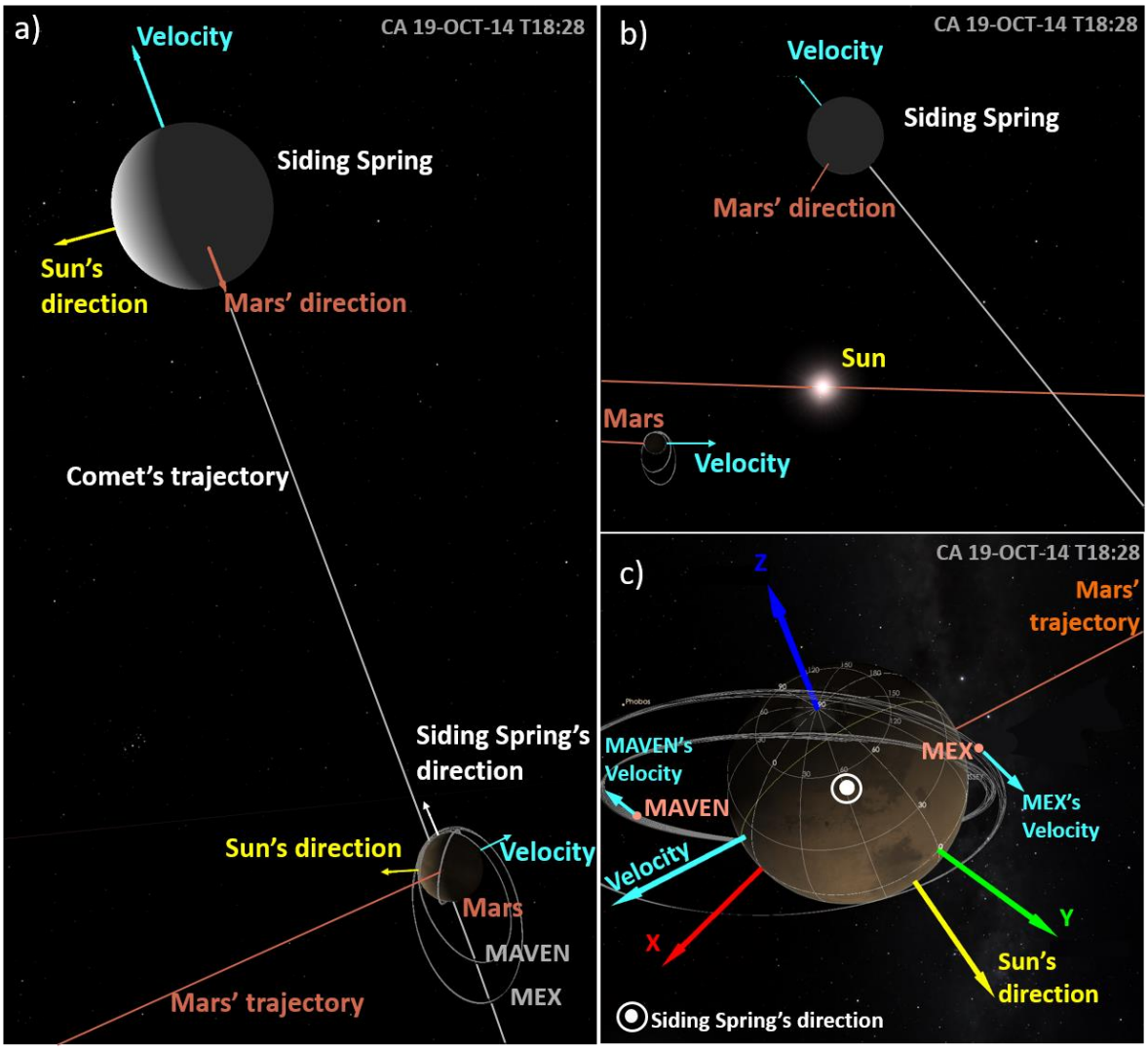

Figure 1: Mars-comet encounter at CA. Siding-Spring had a hyperbolic orbit with an inclination angle of 129° and moved from south to north of the ecliptic at the time of CA, traveling at a relative speed of ~56 km/s. At CA, the comet head relative position with respect to Mars was toward the North and Dawn Martian hemispheres. However, the comet tail that follows the comet was still moving from the south to the north of the ecliptic. Therefore, the southern and dawn Martian hemispheres were the most affected by dust. For better visualization, comet Siding-Spring has been represented as a sphere of radius 15000 km. Panels (a) and (b) are adapted from Sánchez-Cano et al. (2018). (a) Side view of Mars and the comet. (b) View of the Sun, Mars and the comet from behind Mars. (c) Mars as seen from the comet. X, Y and Z are the vector coordinates of Mars in a body fixed frame.

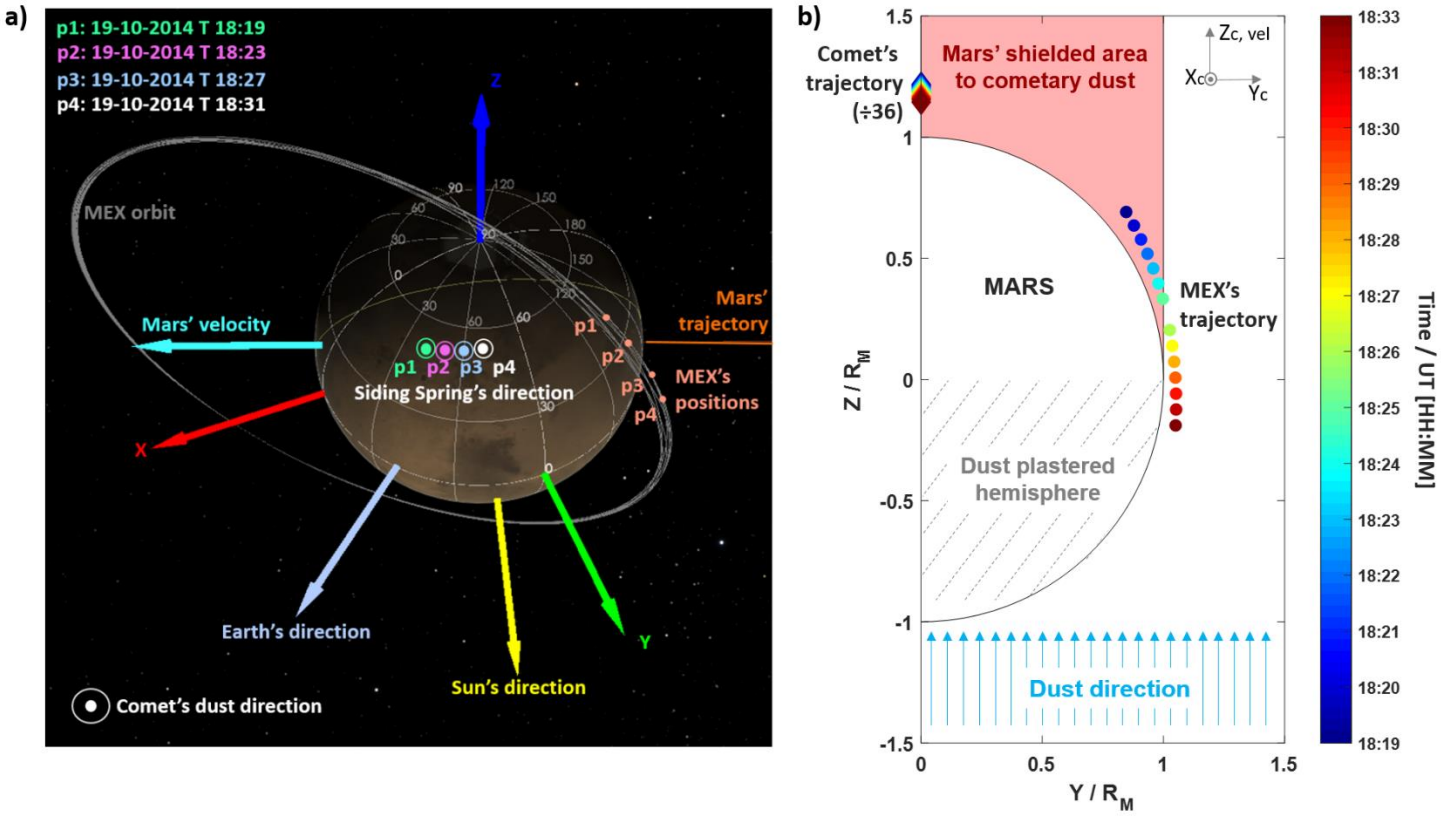

Figure 2: Geometry of the Mars-comet-MEX encounter within an interval of 14 min. (a) Mars and MEX as seen from the comet at 18:19 UT (green), 18:23 UT (pink), 18:27 UT (light blue), and 18:31 UT (white). X, Y, and Z are the vector coordinates of Mars in a body fixed frame. In this figure, the comet's head is northward with respect to Mars (where the readers are). (b) Mars, comet and MEX in the comet velocity frame (Mars's rest frame), where the Zc direction follows the relative velocity vector of the comet with respect to Mars, and Xc points to the Sun. The comet position has been divided by 36 Martian radii for better visualization. While the comet is at the north of Mars (diamonds), the dust tail is still following the comet's head, hitting Mars from the south, specially the southern hemisphere (dust plastered hemisphere). Mars is partly blocking the dust stream and forming a shadow area for dust impacts in the northern hemisphere (reddish cylinder). This shadow cylinder is formed in the direction of their relative velocity vector. Therefore, Mars is shielding MEX up to ~18:25 UT (p1 and p2 in (a)), but not later. In addition to this, we note that the comet's coma is engulfing the whole planet in this figure as its radius is about a million kilometers from the head of the comet.

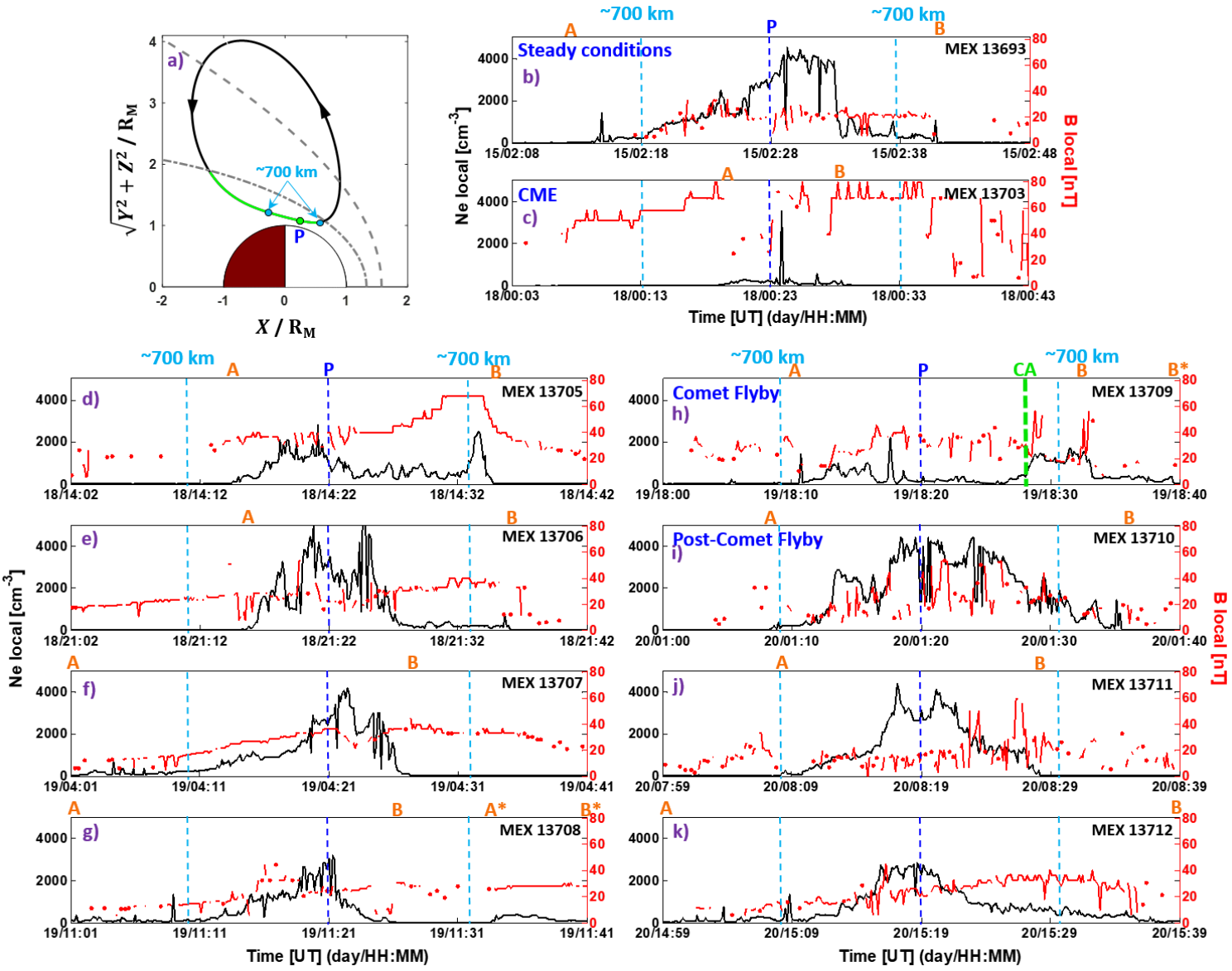

Figure 3: (a) Mars Express trajectory in MSO-cylindrical coordinates (in black), and its transit within the ionosphere cavity (in green). The Sun is to the right. A grey dashed-dotted line indicates the magnetic pileup boundary position (Edberg et al. 2008), and a grey dashed line the bow shock position (Hall et al. 2016). The pericenter is marked with a P and a green dot. The 700 km altitude points are marked with blue dots. (b-k) MARSIS local plasma observations of the ionosphere of Mars at MEX altitude. Each panel shows local electron density (in black) and local magnetic field (in red) from a different orbit. In each panel, the periapsis is indicated with a P and a dark-blue dashed-line, and the times when the orbit was at 700 km are marked with a light-blue dashed-line. A and B correspond to the times at which the local plasma density starts/ends being different from zero. In panel (h), the time of comet CA is also indicated with a green dashed-line. Orbit examples for steady conditions and for the impact of a CME are shown in (b) and (c) respectively.

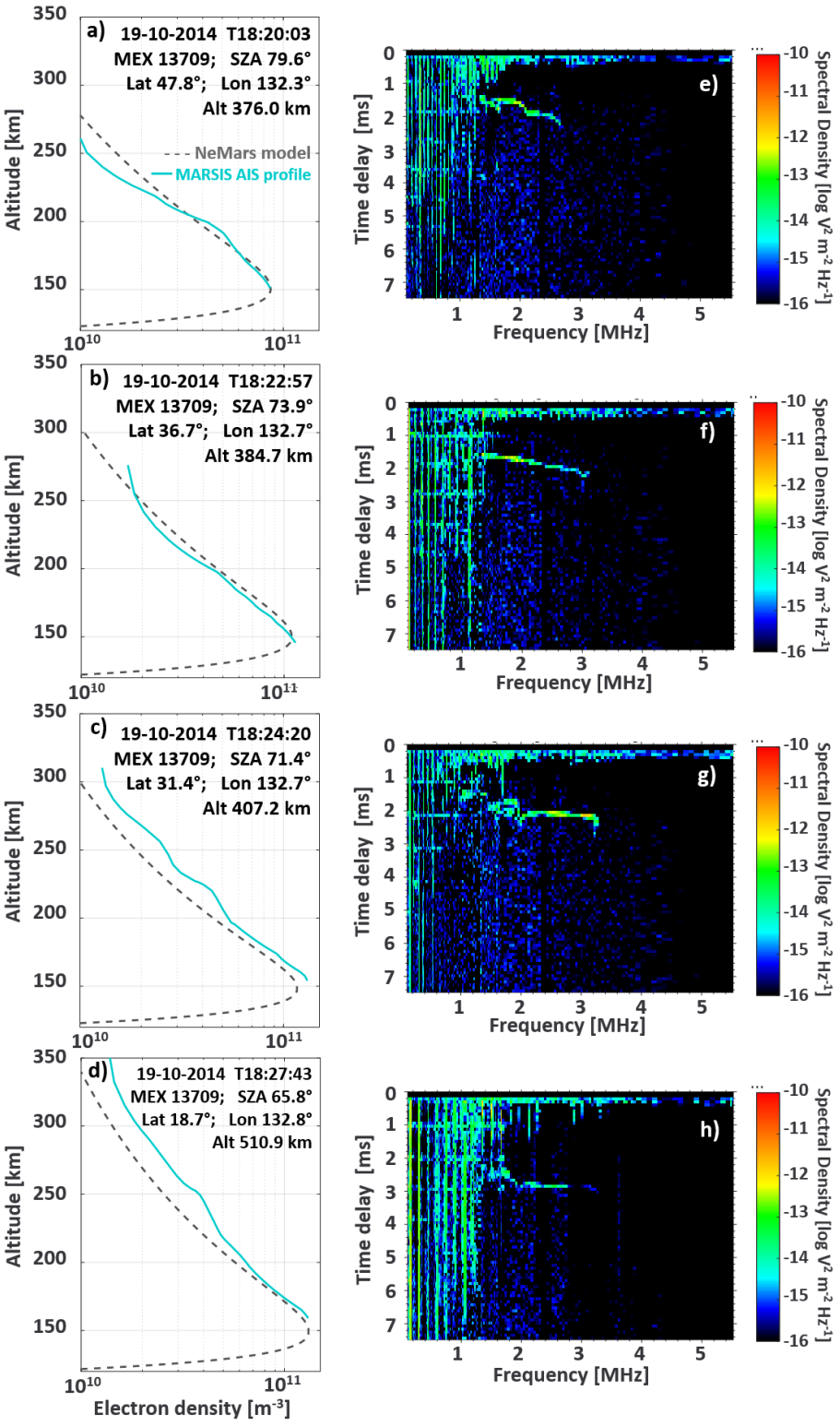

Figure 4: (a-d) Four representative MARSIS-AIS electron density profiles (cyan) from orbit 13709 and the corresponding NeMars profile for reference (gray dashed-line). (e-h) Ionograms from which the electron density profiles in (a-d) were retrieved.

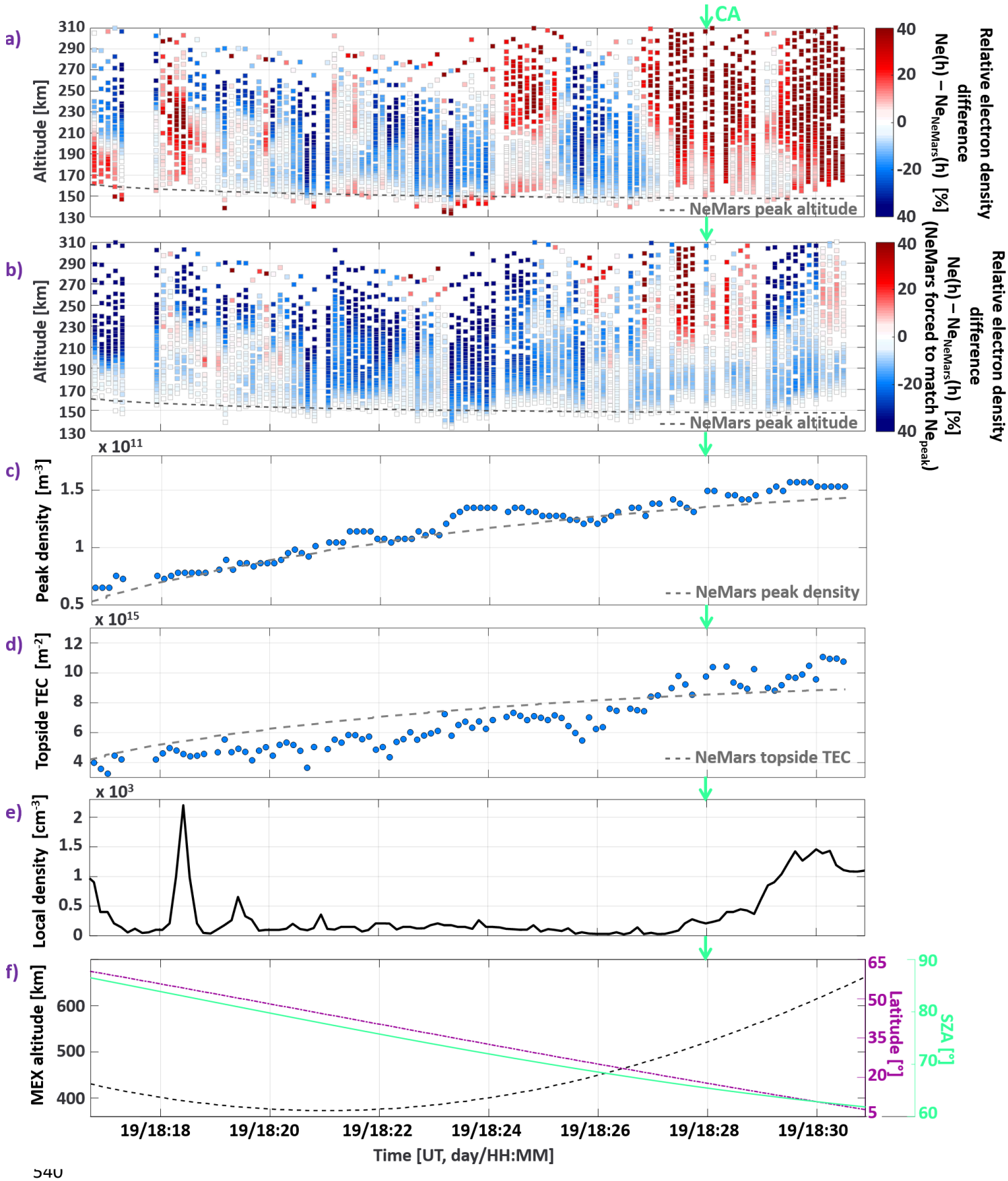
a)
b)
c)
d)
e)
f)
CA
Altitude [km]
NeMars peak altitude
Relative electron density difference
Ne(h) – Ne_NeMars(h) [%]
Ne(h) – Ne_NeMars(h) [%] (NeMars forced to match Ne_peak)
x 10^11
Peak density [m^-3]
NeMars peak density
x 10^15
Topside TEC [m^-2]
NeMars topside TEC
x 10^3
Local density [cm^-3]
MEX altitude [km]
Latitude [°]
SZA [°]
19/18:18
19/18:20
19/18:22
19/18:24
19/18:26
19/18:28
19/18:30
Time [UT, day/HH:MM]

540

Figure 5: Ionospheric parameters for MEX orbit 13709 for SZA<85° and altitude lower than 700 km (where more accurate electron density profiles can be retrieved). (a) Altitude electron density profiles plotted versus time along the MEX orbit. Electron density values are color-coded according to the percentage of density relative variation of the MARSIS-AIS observations with respect to the NeMars model. Reddish colors mean an excess of electron density and blueish colors a density deficit. The NeMars peak altitude is plotted as a gray dashed-line for reference. Discontinuities in each vertical column are caused by different data sampling, as not always it is possible to obtain uniformly spaced data from the ionogram trace. (b) Same than (a) but where NeMars values are forced to fit the AIS peak density. (c) Peak density from AIS profiles. The NeMars peak density is plotted as a gray dashed-line for reference. (d) Topside TEC from AIS profiles. The NeMars topside TEC is plotted as a gray dashed-line for reference. (e) Local plasma density along the orbit (same as Figure 3h). (f) Mars Express altitude (black), latitude (purple) and solar zenith angle (SZA, green).

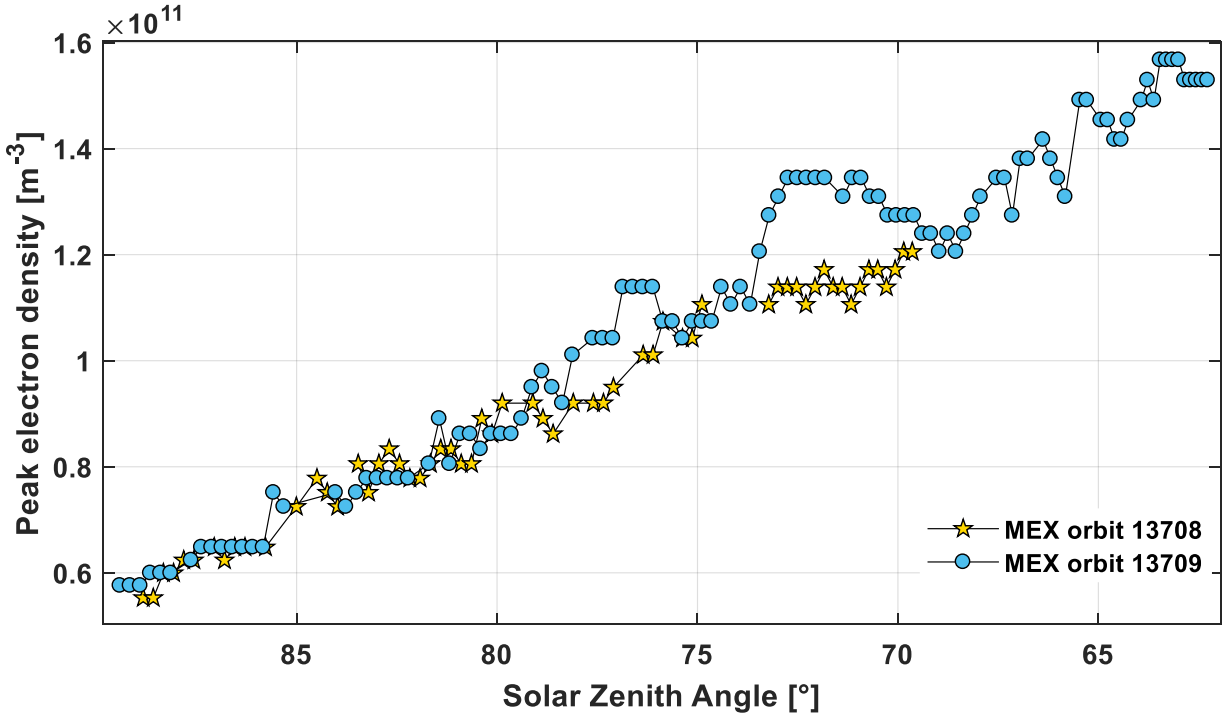

Figure 6: Peak density from AIS profiles from the MEX orbit before the comet encounter (yellow stars) and the orbit of the encounter (blue circles).

References:

- Akalin, F., D.D. Morgan, D.A. Gurnett, D.L. Kirchner, D.A. Brain, R. Modolo, M.H. Acuña, J.R. Espley, (2010), Dayside induced magnetic field in the ionosphere of Mars, *Icarus*, 206, 104–111, doi:10.1016/j.icarus.2009.03.021

- Andersson, L., et al. (2015), Dust observations at orbital altitudes surrounding Mars, *Science*, 350, 6261, doi:10.1126/science.aad0398.

- Andrews, D. J., H. J. Opgenoorth, N. J. T. Edberg, M. Andre, M. Franz, E. Dubinin, F. Duru, D. Morgan, and O. Witasse (2013), Determination of local plasma densities with the MARSIS radar: Asymmetries in the high-altitude Martian ionosphere, J. Geophys. Res. Space Physics, 118, 6228–6242, doi:10.1002/jgra.50593.

- Andrews, D. J., M. André, H. J. Opgenoorth, N. J. T. Edberg, C. Diéval, F. Duru, D. A. Gurnett, D. Morgan, and O. Witasse (2014), Oblique reflections in the Mars Express MARSIS data set: Stable density structures in the Martian ionosphere, J. Geophys. Res. Space Physics, 119, 3944–3960, doi:10.1002/2013JA019697.

- Ao, C. O., C. D. Edwards Jr., D. S. Kahan, X. Pi, S. W. Asmar, and A. J. Mannucci (2015), A first demonstration of Mars crosslink occultation measurements, Radio Sci., 50, doi:10.1002/2015RS005750.

- Benna, M., Mahaffy, P. R., Grebowsky, J. M., Plane, J. M. C., Yelle, R. V., and Jakosky, B.M. (2015). Metallic ions in the upper atmosphere of Mars from the passage of comet C/2013 A1 (Siding Spring). Geophys. Res. Lett., 42, 4670–4675, doi:10.1002/2015GL064159.

- Bhardwaj, A., On the Solar EUV Deposition in the Inner Comae of Comets with Large Gas Production Rates, Geophys. Res. Lett., 30(24), 2244, doi:10.1029/2003GL018495, 2003.

- Bodewits, D., Kelley, M. S. P., Li, J., Farnham, T. L., & A'Hearn, M. F. (2015). The pre-perihelion activity of dynamically new comet C/2013 A1 (Siding Spring) and its close encounter with Mars. The Astrophysical Journal Letters, 802(1), L6. https://doi.org/10.1088/2041-8205/802/1/L6

- Cardnell, S., O. Witasse, G. J. Molina-Cuberos, M. Michael, S. N. Tripathi, G. Déprez, F. Montmessin, and K. O'Brien (2016), A photochemical model of the dust-loaded ionosphere of Mars, J. Geophys. Res. Planets, 121, 2335–2348, doi:10.1002/2016JE005077.

- Cartacci, M., Sánchez-Cano, B., Orosei, R., Noschese, R., Cicchetti, A., Witasse, O., et al. (2018). Improved estimation of Mars ionosphere total electron content. Icarus, 299, 396–410. https://doi.org/10.1016/j.icarus.2017

- Chicarro, A., Martin, P., & Trautner, R. (2004). The Mars Express mission: An overview. In A. Wilson & A. Chicarro (Eds.), Mars Express: The scientific payload (Vol. 1240, pp. 3–13). Noordwijk, Netherlands: ESA Special Publication

- Crismani, M. M. J., et al. (2015). Ultraviolet observations of the hydrogen coma of comet C/2013 A1 (Siding Spring) by MAVEN/IUVS. Geophys. Res. Lett., 42, doi:10.1002/2015GL065290.

- Crismani, M. M. J., Schneider, N. M., Evans, J. S., Plane, J. M. C., Carrillo-Sánchez, J. D., Jain, S., et al. (2018). The impact of comet Siding Spring's meteors on the Martian atmosphere and ionosphere. Journal of Geophysical Research: Planets, 123. https://doi.org/10.1029/2018JE005750

- Duru, F., D. A. Gurnett, T. F. Averkamp, D. L. Kirchner, R. L. Huff, A. M. Persoon, J. J. Plaut, and G. Picardi (2006), Magnetically controlled structures in the ionosphere of Mars, J. Geophys. Res., 111, A12204, doi:10.1029/2006JA011975.

- Edberg, N. J. T., M. Lester, S. W. H. Cowley, and A. I. Eriksson (2008), Statistical analysis of the location of the Martian magnetic pileup boundary and bow shock and the influence of crustal magnetic fields, J. Geophys. Res., 113, A08206, doi:10.1029/2008JA013096.

- Espley, J. R., et al. (2015). A comet engulfs Mars: MAVEN observations of comet Siding Spring's influence on the Martian magnetosphere. Geophys. Res. Lett., 42, 8810–8818, doi:10.1002/2015GL066300.

- Forget, F., Hourdin, F., Fournier, R., Hourdin, C., Talagrand, O., Collins, M., et al. (1999). Improved general circulation models of the Martian atmosphere from the surface to above 80 km. Journal of Geophysical Research, 104, 24,155–24,175.

- Formisano, V., et al., (2005), The Planetary Fourier Spectrometer (PFS) onboard the European Mars Express mission, Planet. Space Sci., 53, 963-974.

- Giuranna, M., et al., (2017), Preliminary analysis of PFS/MEx observations of Comet Siding Spring, EPSC Abstracts, Vol. 11, EPSC2017-749, 2017

- Gronoff, G., Rahmati, A., Wedlund, C. S.,Mertens, C. J., Cravens, T. E., & Kallio, E. (2014). The precipitation of keV energetic oxygen ions at Mars and their effects during the comet Siding Spring approach. Geophysical Research Letters, 41, 4844–4850. https://doi.org/10.1002/2014GL060902

- Gurnett, D. A., et al. (2005), Radar soundings of the ionosphere of Mars, Science, 310, 1929–1933.

- Gurnett, D.A., Huff, R.L., Morgan, D.D., Persoon, A.M., Averkamp, T.F., Kirchner, D.L., Duru, F., Akalin, F., Kopf, A.J., Nielsen, E., Safaeinili, A., Plaut, J.J., Picardi, G., (2008). An overview of radar soundings of the martian ionosphere from the Mars Express spacecraft. Adv. Space Res. 41, 1335–1346. http://dx.doi.org/10.1016/j.asr.2007.01.062.

- Gurnett, D. A., Morgan, D. D., Persoon, A. M., Granroth, L. J., Kopf, A. J., Plaut, J. J., and Green, J. L. (2015). An ionized layer in the upper atmosphere of Mars caused by dust impacts from comet Siding Spring. Geophys. Res. Lett., 42, doi:10.1002/ 2015GL063726.

- Hall, B. E. S., et al. (2016). Annual variations in the Martian bow shock location as observed by the Mars express mission. J. Geophys. Res. Space Physics, 121, doi:10.1002/2016JA023316.

- Ilyushin, Y. A., Orosei, R., Witasse, O., & Sánchez-Cano, B. (2017). CLUSIM: A synthetic aperture radar clutter simulator for planetary exploration. Radio Science, 52. https://doi.org/10.1002/2017RS006265

- JPL Small-Body Database: https://ssd.jpl.nasa.gov/sbdb.cgi?ID=dK13A010

- Kim, S. J., G. S. Orton, C. Dumas, and Y. H. Kim 1996. Infrared spectroscopy of Jupiter's atmosphere after the A and E impacts of Comet Shoemaker–Levy 9. Icarus 120, 326–331.

- Kopf, A.J., Gurnett, D.A., Morgan, D.D., Kirchner, D.L., 2008. Transient layers in the topside ionosphere of Mars. Geophys. Res. Lett. 35, 17102. http://dx.doi.org/10.1029/2008GL034948.

- Kopf, A. J., D. A. Gurnett, G. A. DiBraccio, D. D. Morgan, and J. S. Halekas (2017), The transient topside layer and associated current sheet in the ionosphere of Mars, J. Geophys. Res. Space Physics, 122, doi:10.1002/2016JA023591.

- Maurellis, A.N and Cravens, T.E., (2001), Ionospheric Effects of Comet Shoemaker–Levy 9 Impacts with Jupiter, *Icarus*, 154, 350–371, doi:10.1006/icar.2001.6709.

- Mendillo, M., G. S. Hawkins and J. A. Klobuchar, A sudden vanishing of the ionospheric F region due to the launch of Skylab, J. Geophys. Res., 80, 2217, 1975

- Mendillo, M., The effect of rocket launches on the ionosphere, Adv. Space Res., 1, 275, 1981.

- Moore, L., J. O'Donoghue, I. Müller-Wodarg, M. Galand, M. Mendillo, (2015), Saturn ring rain: Model estimates of water influx into Saturn's atmosphere, *Icarus,* 245, 355-366, http://dx.doi.org/10.1016/j.icarus.2014.08.041

- Morel, L., O. Witasse, R. Warnant, J.-C. Cerisier, P.-L. Blelly, and J. Lilensten (2004), Diagnostic of the dayside ionosphere of Mars using the total electron content measurement by the NEIGE/Netlander experiment: An assessment study, Planet. Space Sci., 52(7), 603–611, doi:10.1016/j.pss.2003.12.007.

- Morgan, D. D., O. Witasse, E. Nielsen, D. A. Gurnett, F. Duru, and D. L. Kirchner (2013), The processing of electron density profiles from the Mars Express MARSIS topside sounder, Radio Sci., 48, 197–207, doi:10.1002/rds.20023.

- Němec, F., Morgan, D. D., Fowler, C. M., Kopf, A. J., Andersson, L., Gurnett, D. A., Andrews, D. J., & Truhlik, V. (2017). Ionospheric electron densities at Mars: Comparison of Mars Express ionospheric sounding and MAVEN local measurements. Journal of Geophysical Research: Space Physics, 122, 12,393– 12,405. https://doi.org/10.1002/2017JA024629

- O'Donoghue, J. et al., 2013. The domination of Saturn's low-latitude ionosphere by ring ''rain''. Nature, 496, (7444), 193–195, http://dx.doi.org/10.1038/nature12049.

- Orosei, R., Jordan, R. L., Morgan, D. D., Cartacci, M., Cicchetti, A., Duru, F., et al. (2015). Mars Advanced Radar for Subsurface and Ionospheric Sounding (MARSIS) after nine years of operation: A summary. Planetary and Space Science, 112, 98–114. https://doi.org/10.1016/j.pss.2014.07.010

- Peter, K., et al. (2014), The dayside ionospheres of Mars and Venus: Comparing a one-dimensional photochemical model with MaRS (Mars Express) and VeRa (Venus Express) observations, Icarus, 233, 66–82, doi:10.1016/j.icarus.2014.01.028.

- Picardi, G., et al. (2004), MARSIS: Mars advanced radar for subsurface and ionosphere sounding, in Mars Express: The Scientific Payload, ESA Spec. Publ., vol. 1240, edited by A. Wilson and A. Chicarro, pp. 51–69, ESA, Noordwijk, Netherlands

- Ramírez-Nicolás, M., B. Sánchez-Cano, O. Witasse, P.-L. Blelly, L. Vázquez, and M. Lester (2016), The effect of the induced magnetic field on the electron density vertical profile of the Mars' ionosphere: A Mars Express MARSIS radar data analysis and interpretation, a case study, Planet. Space Sci., doi:10.1016/j.pss.2016.03.017.

- Restano, M., Plaut, J. J., Campbell, B. A., Gim, Y., Nunes, D., Bernardini, F., Egan, A., Seu, R., and Phillips, R. J. (2015). Effects of the passage of Comet C/2013 A1 (Siding Spring) observed by the Shallow Radar (SHARAD) on Mars Reconnaissance Orbiter. Geophys. Res. Lett., 42, 4663–4669, doi:10.1002/2015GL064150.

- Russell, C.T., Vaisberg, O., 1983. The interaction of the solar wind with Venus. In: Hunten, D.M., Colin, L., Donahue, T.M., Moroz, V.I. (Eds.), Venus. The University of Arizona Press, Tuscon, pp. 873–940.

- Sánchez-Cano, B., O. Witasse,M. Herraiz, S. M. Radicella, J. Bauer, P.-L. Blelly, and G. Rodríguez-Caderot (2012), Retrieval of ionospheric profiles from the Mars Express MARSIS experiment data and comparison with radio-occultation data, Geosci. Instrum. Methods Data Syst., 1, 77–84, doi:10.5194/gi-1-77-2012.

- Sánchez–Cano, B., S. M. Radicella, M. Herraiz, O. Witasse, and G. Rodríguez–Caderot (2013), NeMars: An empirical model of the Martian dayside ionosphere based on Mars Express MARSIS data, Icarus, 225, 236–247, doi:10.1016/j.icarus.2013.03.021.

738 – Sánchez–Cano, B., et al. (2015a), Total electron content in the Martian atmosphere: A critical
739 assessment of the Mars Express MARSIS datasets, J. Geophys. Res. Space Physics, 120, 2166–
740 2182, doi:10.1002/2014JA020630.
741
742 – Sánchez-Cano, B., M. Lester, O. Witasse, S. E. Milan, B. E. S. Hall, P.-L. Blelly, S. M. Radicella, and
743 D. D. Morgan (2015b), Evidence of scale height variations in the Martian ionosphere over the
744 solar cycle, J. Geophys. Res. Space Physics, 120, 10,913–10,925, doi:10.1002/2015JA021949.
745
746 – Sánchez-Cano, B., et al. (2016a), Solar cycle variations in the ionosphere of Mars as seen by
747 multiple Mars Express data sets, J. Geophys. Res. Space Physics, 121, 2547–2568,
748 doi:10.1002/2015JA022281.2016b
749
750 – Sánchez-Cano, B., M. Lester, O. Witasse, P.-L. Blelly, M. Cartacci, S.M. Radicella, M. Herraiz, Solar
751 cycle variations in the ionosphere of Mars, (2016b), Física de la Tierra, publication at
752 Department of Physics of the Earth, Astronomy and Astrophysics I of the Universidad
753 Complutense of Madrid, Spain. Vol. 28, 93-108, ISSN: 0214-4557.
754 http://dx.doi.org/10.5209/rev_FITE.2016.v28.53899
755
756 – Sánchez-Cano, B., et al. (2017). Mars plasma system response to solar wind disturbances
757 during solar minimum. J. Geophys. Res. Space Physics, 122, 6611–6634,
758 doi:10.1002/2016JA023587.
759
760 – Sánchez – Cano, B., Witasse, O., Lester, M., Rahmati, A., Ambrosi, R., Lillis, R., et al. (2018).
761 Energetic particle showers over Mars from comet C/2013 A1 Siding Spring. Journal of
762 Geophysical Research: Space Physics, 123. https://doi.org/10.1029/2018JA025454
763
764 – Schleicher, D., Knight, M., & Skiff, B. (2014). Comet C/2013 A1 (Siding Spring). Bureau
765 Electronic Telegrams, 4004, 1.
766
767 – Schneider, N. M., et al. (2015). MAVEN IUVS observations of the aftermath of the Comet Siding
768 Spring meteor shower on Mars. Geophys. Res. Lett., 42, 4755–4761,
769 doi:10.1002/2015GL063863.
770
771 – Tricarico, P., et al (2014). Delivery of dust grains from comet C/2013 A1 (Siding Spring) to
772 Mars. Astrophys. J. Lett., 787, L35, doi:10.1088/2041-8205/787/2/L35.
773

774 – Venkateswara Rao, N., ManasaMohana, P., Jayaraman, A., and Rao, S. V. B. (2016), Some new
775 aspects of the transient ionization layer of comet Siding Spring origin in the Martian upper
776 atmosphere. J. Geophys. Res. Space Physics, 121, doi:10.1002/2015JA022189.
777
778 – Vigren, E. and Galand, M. Predictions of Ion Production Rates and Ion Number Densities within
779 the Diamagnetic Cavity of Comet 67P/Churyumov-Gerasimenko at Perihelion. The
780 Astrophysical Journal, 772:33, July 2013. doi: 10.1088/0004-637X/772/1/33.
781
782 – Wang, Y. C., Luhmann, J. G., Rahmati, A., Leblanc, F., Johnson, R. E., Cravens, T. E., & Ip, W. H.
783 (2016). Cometary sputtering of the Martian atmosphere during the Siding Spring encounter.
784 Icarus, 272, 301–308. https://doi.org/10.1016/j.icarus.2016.02.040
785
786 – Witasse, O. et al (2017). Interplanetary coronal mass ejection observed at STEREO-A, Mars,
787 comet 67P/Churyumov-Gerasimenko, Saturn, and New Horizons en route to Pluto:
788 Comparison of its Forbush decreases at 1.4, 3.1, and 9.9 AU. J. Geophys. Res. Space Physics,
789 122, doi:10.1002/2017JA023884.
790
791 – Yelle, R.V., A. Mahieux, S. Morrison, V. Vuitton, S.M. Hörst, (2014), Perturbation of the Mars
792 atmosphere by the near-collision with Comet C/2013 A1 (Siding Spring), Icarus, 237, 202–
793 210, http://dx.doi.org/10.1016/j.icarus.2014.03.030

794